APL Materials

Observation of maxon-like ultrasound in elastic metabeam

Peng Zhang ; Yunya Liu ; Keping Zhang ; Yuning Wu ; Fei Chen ; Yi Chen ; Pai Wang ✉ ;
Xuan Zhu ✉

Check for updates

View Online

Export Citation

09 April 2024 09:37:57

AIP Publishing

Observation of maxon-like ultrasound in elastic metabeam

Peng Zhang,[1] Yunya Liu,[2] Keping Zhang,[1] Yuning Wu,[1] Fei Chen,[2] Yi Chen,[3] Pai Wang,[2,a)] and Xuan Zhu[1,a)]

AFFILIATIONS

[1] Department of Civil and Environmental Engineering, University of Utah, Salt Lake City, Utah 84112, USA
[2] Department of Mechanical Engineering, University of Utah, Salt Lake City, Utah 84112, USA
[3] Institute of Applied Physics, Karlsruhe Institute of Technology (KIT), 76128 Karlsruhe, Germany

Note: This paper is part of the Special Topic on New Frontiers in Acoustic and Elastic Metamaterials and Metasurfaces.
[a)]Authors to whom correspondence should be addressed: pai.wang@utah.edu and xuan.peter.zhu@utah.edu

ABSTRACT

We observe maxon-like dispersion of ultrasonic guided waves in elastic metamaterials consisting of a rectangular beam and an array of cylindrical resonators. The pillars act as asymmetric resonators that induce a strong modal hybridization. We experimentally observe the strongly localized maxon mode with zero group velocity. Our study also demonstrates a unique feature of the maxon with a down-shifting peak frequency in space. To reveal the fundamental mechanism, we conduct comprehensive numerical studies on all frieze group symmetries and key geometric parameters.

I. INTRODUCTION

Vibro-elastic metamaterials are engineered heterogeneous composites designed to control the propagation of mechanical waves in solid media. They can enable unconventional phenomena, including frequency bandgap,[1–9] negative refraction,[10–14] and topologically protected mode.[15–20] Moreover, they have a broad range of applications, such as cloaking,[21–26] focusing,[27–30] signal processing,[31,32] and energy harvesting.[33–35] Recently, Chen *et al.*[36,37] presented a new category of elastic metamaterials that support roton-like dispersion relations using non-local interactions beyond the nearest neighbor (BNN). Iglesias Martínez *et al.*[38] then experimentally observed this unique behavior in polymer-based metamaterials, where the dispersion curve exhibits a local minimum similar to the roton behavior,[39–41] which was typically observed in the low-temperature quantum systems, such as helium-4 superfluid.[42–46]

In the metamaterial context, rotons and maxons refer to local minima and local maxima on the fundamental wave mode band (a.k.a. the "acoustical" branch), respectively, at the interior of the first Brillouin zone. They indicate the existence of localized wave modes with a finite phase velocity but zero group velocity (ZGV).[47] These ZGV modes are highly desirable in quantitative nondestructive evaluation and structural health monitoring due to the energy trapping that enhances the signal-to-noise ratio. Historically, Tolstoy and Usdin first predicted the higher mode (a.k.a "optical" branch) ZGV point in an elastic plate.[48] More recently, Prada *et al.* experimentally observed this localized mode.[47] In addition, studies also identified higher-band ZGV modes in a wide range of waveguides, including beams,[49] concrete slabs,[50] rails,[51,52] immersed cylindrical shells,[53] elastic layered structures,[54] and nanoporous silicon.[55] Moreover, these ZGV modes have enabled various applications, such as sub-wavelength thickness measurements,[56] cumulative fatigue damage characterization,[57] multi-layer interfacial stiffness evaluation,[58] and gigahertz imaging of nanoscale bilayer.[59]

In the past two years, three new methods have been proposed to realize roton-like ZGV modes on the acoustical branch in metamaterials, including non-local interactions,[36,60–62] chiral micropolar elasticity,[63,64] and the eigenstrain-based design[65–67] with mono-mode elasticity. However, no study is yet to focus on maxon-like

dispersion and analyze the difference between roton and maxon modes in metamaterials. In this article, we experimentally observe the resonator-induced maxon-like dispersion in a metabeam. The maxon mode differentiates itself from conventional resonator-induced flat bands[3,4] by high selectivity in wavelength. While previous researchers noted a similar dispersion phenomenon that is distinct from flat bandgap,[68,69] our study shows and analyzes, for the first time, the mechanism of maxons in elastic waveguides and the observable difference between rotons and maxons in terms of peak-frequency shifts in space. More importantly, we explain the underlying symmetric breaking requirement for maxon formation in elastic waveguides via numerical simulations.

II. METHODS AND MATERIALS

To investigate the resonator-induced maxon behavior, we design and construct an elastic metabeam consisting of a rectangular beam ($560 \times 10 \times 1$ mm^3) and an array of cylindrical resonators (4 mm diameter and 4 mm height). The elastic metabeam is directly manufactured from a 6061 aluminum alloy block by removing excessive materials. A total of 53 pillar resonators are machined with a spatial interval of 10 mm (center to center), as shown in Fig. 1(a). Both ends of the metabeam are wrapped with clay to suppress possible reflections. We then attach a square lead zirconate titanate (PZT) patch ($10 \times 10 \times 0.52$ mm^3, Navy type II) at one end of the metabeam and apply a broadband voltage excitation onto the PZT to induce vibrations in the frequency from high-audible to ultrasonic spectrum. To capture the maxon-like dispersion behavior, we configure and output a chirp signal with a frequency window from 10 to 60 kHz over 0.3 ms through the arbitrary waveform generator (AWG) module of a PicoScope. For measurements, we use both contact and non-contact sensors to obtain spatial–temporal dynamic responses of the metabeam. As shown in Fig. 1(b), we use a broadband acoustic emission (AE) sensor (Physical Acoustics PICO sensor) to capture the out-of-plane velocity responses (v_z), and we manually move and attach the sensor with wax as the couplant. In addition, as indicated in Fig. 1(c), we also use Polytec's 3D laser vibrometer CLV-3230 to extract all three velocity responses (v_x, v_y, and v_z) from the metabeam. A retro-reflective

tape is attached to the scanning surface of the beam to increase the reflectivity and improve the signal strength, and a sensitivity of 5 mm s^{-1} V^{-1} is adopted for measurements. We further design and manufacture a motion platform to host the metabeam and facilitate laser scanning. Using both AE sensor and laser vibrometer, we first extract vibration responses from the top surface of each of the first 39 pillars with a spatial sampling interval of 10 mm. Next, we also extract responses at the bottom of the substrate beam within the same region with an interval of 5 mm, which allows us to estimate the experimental dispersion relations of the metabeam. All measurements are sampled with a time step of 0.025 μs over a period of 20 ms and repeated ten times with a PicoScope oscilloscope before getting averaged, digitized, and stored for further analysis.

We also establish finite-element models on the COMSOL software platform to investigate the underlying mechanism and special characteristics of resonator-induced maxon-like dispersion and the behavior of the localized mode. First, an eigenanalysis is performed to calculate the dispersion curves of the designed metabeam. We apply the Bloch-wave boundary conditions in the wave propagation direction (x−axis) on a unit cell composed of the base beam and a pillar resonator. The material model of the beam and pillar is set as aluminum with Young's modulus E = 70 GPa, Poisson's ratio v = 0.33, and density ρ = 2700 kg/m^3. We sweep the wavenumber in the first Brillouin zone to obtain dispersion curves, which are plotted as shown in Fig. 1(d). The highlighted dispersion curve demonstrates a maximum frequency at ~38.3 kHz and 15.75 m^{-1}. This local maximum point hosts the localized maxon ZGV mode. Moreover, we quantify the mode shape patterns based on the longitudinal and vertical bending displacement ratio. To categorize the modal shapes, here, we adopt the symmetry of a bare beam, where two axes of symmetry on the cross-sectional plane separate the guided waves into four mode families,[70] namely, longitudinal (L) mode, vertical bending (B_y) mode, horizontal bending (B_z) mode, and torsional (T) mode, for a wavevector along the propagation direction (x−axis). The bending modes are named based on the axis the bending motions are about. The resonators on the bare beam would interact with the beam and thus modify these wave modes. As shown in Fig. 1(d), the maxon emerges when the L-dominant branch meets
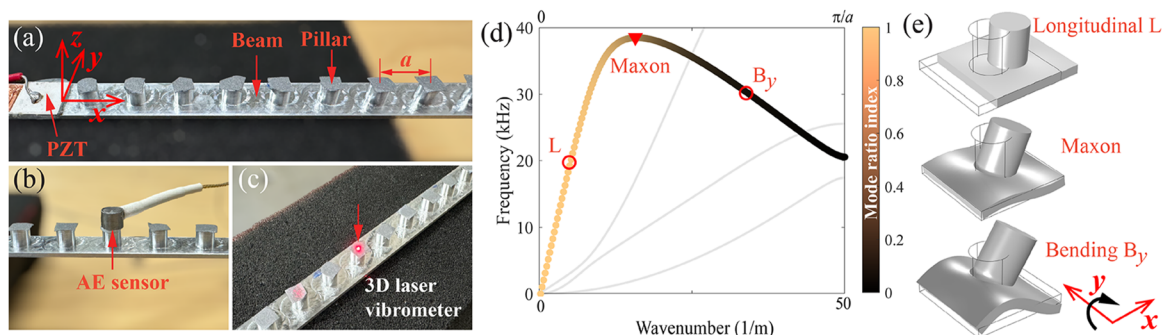
FIG. 1. Experimental setup and eigenanalysis to study the maxon in a metabeam. (a) The metabeam design with a pillar spacing of a = 10 mm and the coordinate system, (b) contact measurements using a broadband acoustic emission sensor, (c) non-contact measurements using a laser Doppler vibrometer, (d) dispersion curves of the metabeam, and the colorbar is based on the mode ratio index, R, which quantifies the participation of L and B_y modes (see the supplementary material), and (e) L-dominant, maxon, and B_y-dominant mode shapes.

the B_y-dominant branch. This dispersion curve is color-coded based on the mode ratio index R, for which $R = 1$ indicates the pure L mode and $R = 0$ indicates the pure B_y mode. Detailed calculation procedures are described in the supplementary material. We find that the maxon mode is very close to but not exactly at the point of R = 0.5, which denotes the equal participation of the L and B_y modes. Representative mode shapes in Fig. 1(e) illustrate the effects of the pillar resonator, which couples the L and B_y modes in the bare beam together to form the hybridized maxon mode in the metabeam. Furthermore, we conduct time-dependent finite-element simulations with a metabeam composed of 53 units. A displacement excitation of a chirp signal with a frequency sweeping from 10 to 60 kHz is introduced on one end of the metabeam, and a low-reflecting boundary is applied on the other end to suppress boundary reflections. The Courant–Friedrichs–Lewy (CFL) condition with CFL = 0.2 is satisfied with an element size of 0.5 mm, a time step of 1 μs, and a total simulation time of 4 ms. We extract all three velocity components from the top surface of pillars and the base beam. To obtain dispersion relations from this calculation, we perform two-dimensional fast Fourier transform (2D-FFT) on spatial–temporal sampling of the wavefield along the metabeam; velocity components extracted close to the excitation source are used to study the localized energy trapping and maximum frequency behavior of the maxon. Consistent with the experiment, dynamic responses at the center of the top surface of the first 39 pillars were extracted with a spatial sampling interval of 10 mm; the velocities along the center at the back of the base beam were extracted with a spatial sampling interval of 5 mm to cover the same region of the first 39 pillars. Moreover, dynamic responses within the distance of half the maxon wavelength from the excitation source were considered for local resonance measurements.[47]

III. RESULTS AND DISCUSSION

In Figs. 2(a), 2(c), 2(e), and 2(g), the red dotted lines represent the dispersion curves from the single-unit-cell computation based on Bloch's theorem, while the green dashed line indicates the boundary between the first and second Brillouin zones. On top of those, we present the dispersion relations as color intensity plots from finite-size time-dependent analysis in Figs. 2(a) and 2(e). The corresponding results from experimental measurements are shown in Figs. 2(c) and 2(g). Local resonance spectra collected close to the excitation source (within half the wavelength of the maxon) are shown in Figs. 2(b), 2(d), 2(f), and 2(h). Specifically, Figs. 2(b) and 2(d) are based on the in-plane velocities v_x extracted from the top of the first and second pillars that are 5 and 15 mm away from the excitation/origin, respectively; Figs. 2(f) and 2(h) are based on the out-of-plane velocities v_z extracted from the base beam that is 10 and 15 mm away from the excitation/origin, respectively.

We first analyze the results in Figs. 2(a) and 2(c), which are based on in-plane velocities (v_x) at the top surface of pillars. Here, the forward-propagating L-dominant mode with wavenumber from 0 to 15.75 m^{-1} is observed since the L mode has a strong in-plane component. A narrow horizontal strip is identified close to the maxon frequency, from both simulation and experiment, indicating local energy trapping of the maxon mode. The corresponding frequency responses measured in the vicinity of the source, as shown
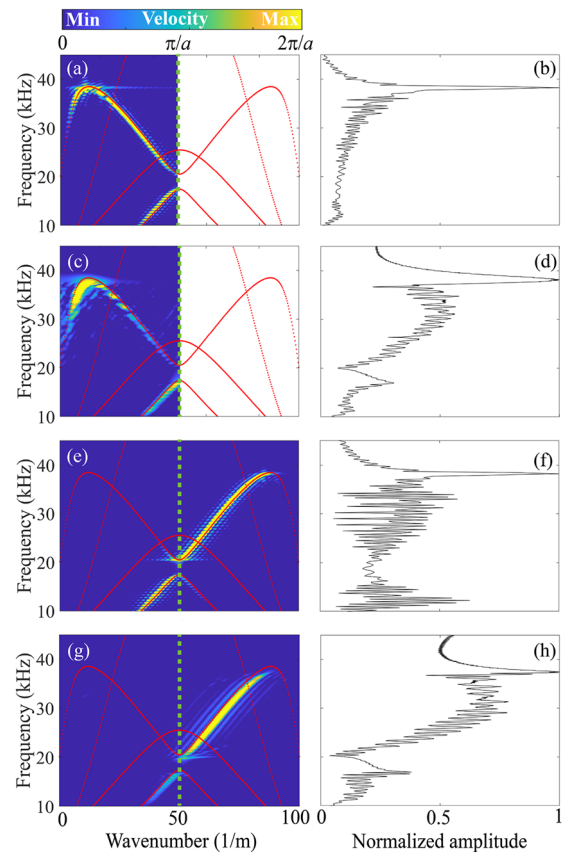
FIG. 2. (a) Dispersion relations and (b) local resonance spectrum based on velocity component v_x extracted from pillars in the numerical model; (c) dispersion relations and (d) local resonance spectrum based on velocity component v_x extracted from pillars in experiment; (e) dispersion relations and (f) local resonance spectrum based on velocity component v_z extracted from the base beam in the numerical model; (g) dispersion relations and (h) local resonance spectrum based on velocity component v_z extracted from the base beam in experiment. The red dotted lines represent the theoretical dispersion curves, and the vertical green dashed lines indicate the boundary of the first Brillouin zone.

in Figs. 2(b) and 2(d), exhibit a clear resonant peak aligned with the maxon frequency near 38.3 kHz, providing strong evidence supporting the localized nature of the maxon mode. Then, we investigate the dispersion relations in Figs. 2(e) and 2(g), which are based on out-of-plane velocities (v_z) collected at the bottom surface of the beam. We note that the forward-propagating waves with positive group velocity are more pronounced since we sample the dynamic responses along the +x direction in both model and experiment.[71] As expected, out-of-plane motions highlight the forward-propagating wave modes at the B_y-dominant branch, which extends beyond the first Brillouin zone. Their corresponding frequency responses in Figs. 2(f) and 2(h) also exhibit a clear resonant peak at the maxon frequency. In general, Fig. 2 shows that the maxon resonance results from standing waves formed by interference between the counter-propagating L-dominant and B_y-dominant modes.

Next, we investigate the non-propagating nature of the maxon mode, focusing on the spatial distribution of the velocity field near
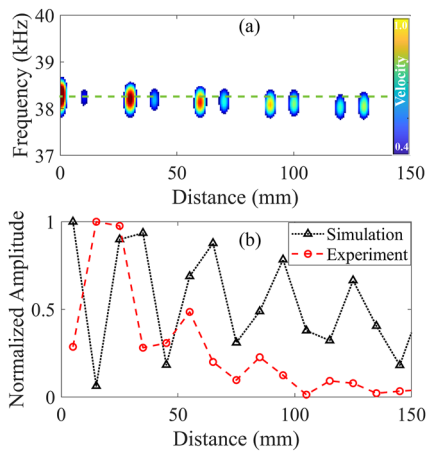
FIG. 3. (a) Spatial distribution of out-of-plane velocity (v_z) at the base beam using the finite element model demonstrating local maximum frequency and energy trapping. (b) Amplitude of dynamic responses based on in-plane velocity (v_x) at the pillars from simulation and experiment at their peak frequencies, respectively.

the source around the maxon frequency. For the numerical model, the out-of-plane velocity components extracted from 300 scanning points along the center at the base beam are processed. The numerical results, as shown in Fig. 3(a), illustrate a series of discrete high-amplitude anti-nodes in spectral data with increasing distance. The spectral component at the maxon frequency is trapped close to the excitation source, and the peak frequencies drop with increasing distance from the source. Lower frequency peaks away from the source are attributed to the interference between two slowly propagating guided wave modes on both sides of the local maximum (i.e., maxon) of dispersion. The distance between adjacent spectral anti-nodes is approximately half of the maxon wavelength ($\lambda/2 = 31.7$ mm). Figure 3(b) presents the numerical and experimental normalized amplitude profiles extracted from the center of the top of the pillars at the maxon frequency with a reasonable agreement (38.4 kHz for simulation and 38.3 kHz for experiment). Both the simulation and experimental results demonstrate that high-amplitude dynamic responses in the vicinity of the maxon frequency are trapped within

half the maxon wavelength (31.7 mm) from the excitation source. Moreover, the distance between peaks is approximately equivalent to half the maxon wavelength in both the simulation and experiment. The discrepancies between the simulation and experimental results can be attributed to residual stresses, manufacturing errors, and damping effects. We note that, while maxon and roton modes share many similarities, the peak-frequency down-shift observed here is a unique feature of maxon-like dispersion, as the roton-like dispersion would result in a peak-frequency up-shift away from the excitation source.[47,52]

In addition, we numerically study the relation between the maxon-like dispersion and the symmetries in the metabeam design. To simplify the problem, we focus on 2D designs with the plane-strain formulation, and we apply the quasiperiodic Bloch-wave-type boundary conditions to study each unit cell. Seven different designs are depicted in Figs. 4(a)–4(g). Each represents a different pattern in terms of symmetry. Collectively, they exhaust the list of all possible symmetries (i.e., the frieze groups[72]) of two-dimensional patterns that are periodic in one direction. We specify each design with the naming convention set by the International Union of Crystallography (IUCr):[73] p for primitive unit cell, m for reflection (vertical denoted first), g for glide-reflection, and number 1 or 2 for the highest order of symmetry.

As highlighted by the light blue lines in Figs. 4(h)–4(n), only four out of seven designs based on the frieze groups manifest the maxon-like dispersion relations. This shows that maxon modes cannot be simply achieved by any locally resonant metamaterials. In fact, most of the resonant designs[3,4,74] exhibit a flat band (ZGV modes for a wide range of wavenumbers) instead of a local maximum (ZGV mode for one particular wavenumber) near the resonant frequency. There is a key difference here: a flat band indicates a strong localization of wave modes over a range of different wavelengths, while the maxon-like dispersion has the distinctive advantage of selecting a unique wavelength of wave localization. A close scrutiny of the frieze-group-based designs reveals that additional symmetry breaking is needed for maxon formation. For designs shown in Figs. 4(c), 4(e), and 4(g), there exists a symmetry between the top and bottom resonators: they are attached to the base plate at exactly the same lateral location. This results in orthogonality between the L and B_y modes. Hence, this symmetry prevents modal
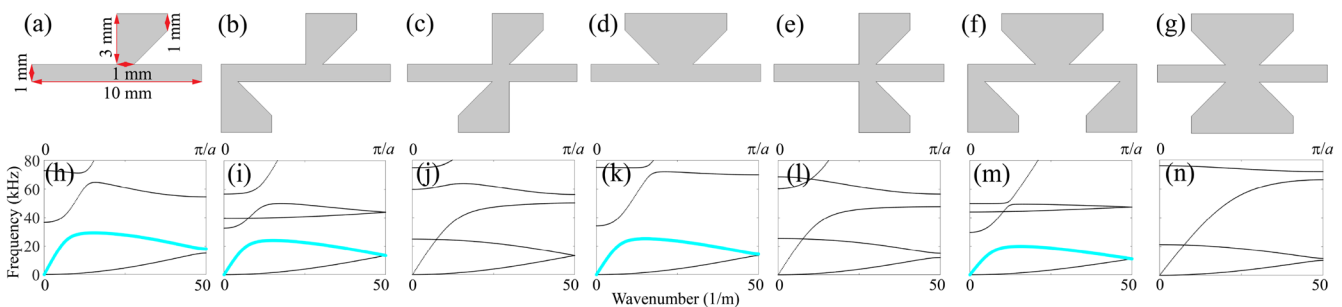
FIG. 4. Designs (a)–(g) based on Frieze groups and their dispersion curves (h)–(n): (a) $p1$ translation only; (b) $p11g$ translation and glide-reflection; (c) $p2$ translation and 180° rotation; (d) $p1m1$ translation and vertical line reflection; (e) $p11m$ translation, horizontal line reflection, and glide-reflection; (f) $p2mg$ translation, 180° rotation, vertical line reflection, and glide-reflection; and (g) $p2mm$ translation, 180° rotation, horizontal line reflection, vertical line reflection, and glide-reflection. The maxon-like dispersion curves are highlighted in light blue in (h), (i), (k), and (m).

hybridization, and no maxon can be formed. Additional parametric studies (see the supplementary material) also provide further evidence supporting this assertion relating symmetry-breaking to modal hybridization and maxon creation.

IV. CONCLUSION

In conclusion, we observe the unique resonator-induced maxon-like dispersion in an elastic metabeam. We demonstrate that longitudinal (L) and bending (B_y) wave modes approximately equally participate in the localized vibration mode at the maxon point. Our numerical calculations and experimental measurements provide compelling evidence for the formation of maxon by modal hybridization. The analysis of the spatial–temporal sampling of the wavefield reveals the unique feature of peak-frequency down-shift in space around the maxon frequency. This behavior is different from roton modes reported in all existing studies. Furthermore, we explain the underlying symmetry-breaking mechanism that enables the formation of maxon-like dispersion. In addition, through parametric studies presented in the supplementary material, we can achieve tunable maxons at a range of different frequencies and wavenumbers by altering the resonator design. This study illuminates the fundamental aspects of localized modes in metamaterials. It paves a new avenue for artificially inducing localized wave modes with highly selective frequency and wavelength. This may potentially become a crucial addition to the toolsets for structural condition assessment and energy harvesting.

SUPPLEMENTARY MATERIAL

For more details, see the supplementary material.

AUTHOR DECLARATIONS

Conflict of Interest

The authors have no conflicts to disclose.

Author Contributions

Peng Zhang: Data curation (equal); Formal analysis (equal); Investigation (equal); Methodology (equal); Software (equal); Validation (equal); Visualization (equal); Writing – original draft (equal); Writing – review & editing (equal). **Yunya Liu**: Formal analysis (equal); Investigation (equal); Methodology (equal); Writing – original draft (equal). **Keping Zhang**: Data curation (equal); Investigation (equal); Methodology (equal). **Yuning Wu**: Formal analysis (equal); Investigation (equal); Methodology (equal); Software (equal); Visualization (equal). **Fei Chen**: Data curation (equal); Visualization (equal); Writing – original draft (equal). **Yi Chen**: Conceptualization (equal); Formal analysis (equal); Writing – review & editing (equal). **Pai Wang**: Conceptualization (equal); Data curation (equal); Formal analysis (equal); Investigation (equal); Methodology (equal); Resources (equal); Software (equal); Supervision (equal); Validation (equal); Visualization (equal); Writing – original draft (equal); Writing – review & editing (equal). **Xuan Zhu**: Conceptualization (equal); Data curation (equal); Formal analysis (equal); Funding acquisition (equal); Investigation (equal); Methodology (equal); Project administration (equal); Resources (equal); Supervision (equal); Validation (equal); Visualization (equal); Writing – original draft (equal); Writing – review & editing (equal).

DATA AVAILABILITY

The data that support the findings of this study are available from the corresponding author upon reasonable request.

REFERENCES

[1]M. Sigalas and E. N. Economou, "Band structure of elastic waves in two dimensional systems," Solid State Commun. **86**, 141–143 (1993).

[2]M. S. Kushwaha, P. Halevi, L. Dobrzynski, and B. Djafari-Rouhani, "Acoustic band structure of periodic elastic composites," Phys. Rev. Lett. **71**, 2022 (1993).

[3]Z. Liu, X. Zhang, Y. Mao, Y. Zhu, Z. Yang, C. T. Chan, and P. Sheng, "Locally resonant sonic materials," Science **289**, 1734–1736 (2000).

[4]P. Wang, F. Casadei, S. Shan, J. C. Weaver, and K. Bertoldi, "Harnessing buckling to design tunable locally resonant acoustic metamaterials," Phys. Rev. Lett. **113**, 014301 (2014).

[5]S. G. Konarski, C. J. Naify, and C. A. Rohde, "Buckling-induced reconfigurability in underwater acoustic scatterers," Appl. Phys. Lett. **116**, 051903 (2020).

[6]C. L. Willey, V. W. Chen, D. Roca, A. Kianfar, M. I. Hussein, and A. T. Juhl, "Coiled phononic crystal with periodic rotational locking: Subwavelength Bragg band gaps," Phys. Rev. Appl. **18**, 014035 (2022).

[7]I. Arretche and K. H. Matlack, "Physical realization and experimental validation of effective phononic crystals for control of radial torsional waves," J. Sound Vib. **540**, 117305 (2022).

[8]C. Widstrand, N. Kalantar, and S. Gonella, "Bandgap tuning in kerfed metastrips under extreme deformation," Extreme Mech. Lett. **53**, 101693 (2022).

[9]W. Ding, T. Chen, C. Chen, D. Chronopoulos, J. Zhu, and B. Assouar, "Thomson scattering-induced bandgap in planar chiral phononic crystals," Mech. Syst. Signal Process. **186**, 109922 (2023).

[10]A. Sukhovich, L. Jing, and J. H. Page, "Negative refraction and focusing of ultrasound in two-dimensional phononic crystals," Phys. Rev. B **77**, 014301 (2008).

[11]N. Kaina, F. Lemoult, M. Fink, and G. Lerosey, "Negative refractive index and acoustic superlens from multiple scattering in single negative metamaterials," Nature **525**, 77–81 (2015).

[12]L. Fang and M. J. Leamy, "Negative refractive index in a two-dimensional nonlinear rotator lattice," Int. Des. Eng. Tech. Conf. Comput. Inf. Eng. Conf. **85475**, V010T10A002 (2021).

[13]H. Danawe and S. Tol, "Experimental realization of negative refraction and subwavelength imaging for flexural waves in phononic crystal plates," J. Sound Vib. **518**, 116552 (2022).

[14]L. Fang and M. Leamy, "Harnessing rotational geometry to design reconfigurable dispersion and refractive index in nonlinear acoustic metamaterials," J. Acoust. Soc. Am. **151**, A39 (2022).

[15]P. Wang, L. Lu, and K. Bertoldi, "Topological phononic crystals with one-way elastic edge waves," Phys. Rev. Lett. **115**, 104302 (2015).

09 April 2024 09:37:57

[16]L. M. Nash, D. Kleckner, A. Read, V. Vitelli, A. M. Turner, and W. T. Irvine, "Topological mechanics of gyroscopic metamaterials," Proc. Natl. Acad. Sci. U. S. A. **112**, 14495–14500 (2015).

[17]H. Danawe, H. Li, K. Sun, and S. Tol, "Finite-frequency topological Maxwell modes in mechanical self-dual kagome lattices," Phys. Rev. Lett. **129**(20), 204302 (2022).

[18]K. Ding, C. Fang, and G. Ma, "Non-Hermitian topology and exceptional-point geometries," Nat. Rev. Phys. **4**, 745–760 (2022).

[19]M. Charara, J. McInerney, K. Sun, X. Mao, and S. Gonella, "Omnimodal topological polarization of bilayer networks: Analysis in the Maxwell limit and experiments on a 3D-printed prototype," Proc. Natl. Acad. Sci. U. S. A. **119**, e2208051119 (2022).

[20]P. A. Deymier, K. Runge, A. Khanikaev, and A. Alù, "Pseudo-spin polarized one-way elastic wave eigenstates in one-dimensional phononic superlattices," Crystals **14**, 92 (2024).

[21]S. A. Cummer and D. Schurig, "One path to acoustic cloaking," New J. Phys. **9**, 45 (2007).

[22]M. Farhat, S. Guenneau, S. Enoch, and A. B. Movchan, "Cloaking bending waves propagating in thin elastic plates," Phys. Rev. B **79**, 033102 (2009).

[23]H. Nassar, Y. Chen, and G. Huang, "Polar metamaterials: A new outlook on resonance for cloaking applications," Phys. Rev. Lett. **124**, 084301 (2020).

[24]X. Xu, C. Wang, W. Shou, Z. Du, Y. Chen, B. Li, W. Matusik, N. Hussein, and G. Huang, "Physical realization of elastic cloaking with a polar material," Phys. Rev. Lett. **124**, 114301 (2020).

[25]F. Martinez and M. Maldovan, "Metamaterials: Optical, acoustic, elastic, heat, mass, electric, magnetic, and hydrodynamic cloaking," Mater. Today Phys. **27**, 100819 (2022).

[26]C. Xu, K. Lyu, and Y. Wu, "Artificial double-zero-index materials," Europhys. Lett. **141**, 15002 (2022).

[27]S. Yang, J. H. Page, Z. Liu, M. L. Cowan, C. T. Chan, and P. Sheng, "Focusing of sound in a 3D phononic crystal," Phys. Rev. Lett. **93**, 024301 (2004).

[28]T. Liu, F. Chen, S. Liang, H. Gao, and J. Zhu, "Subwavelength sound focusing and imaging via gradient metasurface-enabled spoof surface acoustic wave modulation," Phys. Rev. Appl. **11**, 034061 (2019).

[29]C. Xu, G. Okudan, H. Danawe, D. Ozevin, and S. Tol, "Lamb wave focusing by gradient-index phononic crystal lens in layered composites," Proc. SPIE **12047**, 120470J (2022).

[30]G. Okudan, C. Xu, H. Danawe, S. Tol, and D. Ozevin, *Improved Detection of Localized Damage in Pipe-Like Structures Using Gradient-Index Phononic Crystal Lens* (Springer, 2023), pp. 292–299.

[31]P. Karki and J. Paulose, "Stopping and reversing sound via dynamic dispersion tuning in a phononic metamaterial," Phys. Rev. Appl. **15**, 034083 (2021).

[32]N. Kruss and J. Paulose, "Nondispersive one-way signal amplification in sonic metamaterials," Phys. Rev. Appl. **17**, 024020 (2022).

[33]M. Carrara, M. Cacan, M. Leamy, M. Ruzzene, and A. Erturk, "Dramatic enhancement of structure-borne wave energy harvesting using an elliptical acoustic mirror," Appl. Phys. Lett. **100**, 204105 (2012).

[34]J. M. De Ponti, A. Colombi, E. Riva, R. Ardito, F. Braghin, A. Corigliano, and R. V. Craster, "Experimental investigation of amplification, via a mechanical delay-line, in a rainbow-based metamaterial for energy harvesting," Appl. Phys. Lett. **117**, 143902 (2020).

[35]M. Alshaqaq, C. Sugino, and A. Erturk, "Programmable rainbow trapping and band-gap enhancement via spatial group-velocity tailoring in elastic metamaterials," Phys. Rev. Appl. **17**, L021003 (2022).

[36]Y. Chen, M. Kadic, and M. Wegener, "Roton-like acoustical dispersion relations in 3D metamaterials," Nat. Commun. **12**(1), 3278 (2021).

[37]M. Groß, J. Schneider, Y. Chen, M. Kadic, and M. Wegener, "Dispersion engineering by hybridizing the back-folded soft mode of monomode elastic metamaterials with stiff acoustic modes," Adv. Mater. **36**, 2307553 (2023).

[38]J. A. Iglesias Martínez, M. F. Groß, Y. Chen, T. Frenzel, V. Laude, M. Kadic, and M. Wegener, "Experimental observation of roton-like dispersion relations in metamaterials," Sci. Adv. **7**, eabm2189 (2021).

[39]L. Landau, "Theory of the superfluidity of helium II," Phys. Rev. **60**, 356 (1941).

[40]E. B. Kolomeisky, J. Colen, and J. P. Straley, "Negative group velocity and Kelvin-like wake pattern," Phys. Rev. B **105**, 054509 (2022).

[41]L. Chomaz, R. M. van Bijnen, D. Petter, G. Faraoni, S. Baier, J. H. Becher, M. J. Mark, F. Wächtler, L. Santos, and F. Ferlaino, "Observation of roton mode population in a dipolar quantum gas," Nat. Phys. **14**, 442–446 (2018).

[42]R. P. Feynman, "Atomic theory of the two-fluid model of liquid helium," Phys. Rev. **94**, 262 (1954).

[43]D. Henshaw and A. Woods, "Modes of atomic motions in liquid helium by inelastic scattering of neutrons," Phys. Rev. **121**, 1266 (1961).

[44]M. S. Bryan and P. E. Sokol, "Maxon and roton measurements in nanoconfined ^{4}He," Phys. Rev. B **97**, 184511 (2018).

[45]H. Godfrin, K. Beauvois, A. Sultan, E. Krotscheck, J. Dawidowski, B. Fåk, and J. Ollivier, "Dispersion relation of Landau elementary excitations and thermodynamic properties of superfluid ^{4}He," Phys. Rev. B **103**, 104516 (2021).

[46]N. P. Müller and G. Krstulovic, "Critical velocity for vortex nucleation and roton emission in a generalized model for superfluids," Phys. Rev. B **105**, 014515 (2022).

[47]C. Prada, D. Clorennec, and D. Royer, "Local vibration of an elastic plate and zero-group velocity lamb modes," J. Acoust. Soc. Am. **124**, 203–212 (2008).

[48]I. Tolstoy and E. Usdin, "Wave propagation in elastic plates: Low and high mode dispersion," J. Acoust. Soc. Am. **29**, 37–42 (1957).

[49]K. Zhang, R. Cui, Y. Wu, L. Zhang, and X. Zhu, "Extraction and selective promotion of zero-group velocity and cutoff frequency resonances in bi-dimensional waveguides using the electromechanical impedance method," Ultrasonics **131**, 106937 (2023).

[50]Y.-T. Tsai and J. Zhu, "Simulation and experiments of airborne zero-group-velocity lamb waves in concrete plate," J. Nondestruct. Eval. **31**, 373–382 (2012).

[51]Y. Wu, R. Cui, K. Zhang, X. Zhu, and J. S. Popovics, "On the existence of zero-group velocity modes in free rails: Modeling and experiments," NDT & E Int. **132**, 102727 (2022).

[52]Y. Wu, K. Zhang, P. Zhang, X. Zhu, and J. S. Popovics, "Dynamic behavior of a zero-group velocity guided mode in rail structures," JASA Express Lett. **3**, 105601 (2023).

[53]S. Agounad, E. H. Aassif, Y. Khandouch, D. Décultot, G. Maze, and A. Elhanaoui, "Acoustic scattering from immersed composite cylindrical shells: Existence of zero group velocity circumferential waves," Compos. Struct. **182**, 12–24 (2017).

[54]E. Glushkov and N. Glushkova, "Multiple zero-group velocity resonances in elastic layered structures," J. Sound Vib. **500**, 116023 (2021).

[55]M. Thelen, N. Bochud, M. Brinker, C. Prada, and P. Huber, "Laser-excited elastic guided waves reveal the complex mechanics of nanoporous silicon," Nat. Commun. **12**, 3597 (2021).

[56]M. Cès, D. Clorennec, D. Royer, and C. Prada, "Thin layer thickness measurements by zero group velocity lamb mode resonances," Rev. Sci. Instrum. **82**, 114902 (2011).

[57]G. Yan, S. Raetz, N. Chigarev, J. Blondeau, V. E. Gusev, and V. Tournat, "Cumulative fatigue damage in thin aluminum films evaluated non-destructively with lasers via zero-group-velocity lamb modes," NDT & E Int. **116**, 102323 (2020).

[58]S. Mezil, J. Laurent, D. Royer, and C. Prada, "Non contact probing of interfacial stiffnesses between two plates by zero-group velocity Lamb modes," Appl. Phys. Lett. **105**, 021605 (2014).

[59]Q. Xie, S. Mezil, P. H. Otsuka, M. Tomoda, J. Laurent, O. Matsuda, Z. Shen, and O. B. Wright, "Imaging gigahertz zero-group-velocity lamb waves," Nat. Commun. **10**, 2228 (2019).

[60]C. Coulais, C. Kettenis, and M. van Hecke, "A characteristic length scale causes anomalous size effects and boundary programmability in mechanical metamaterials," Nat. Phys. **14**, 40–44 (2018).

[61]P. Ziemke, T. Frenzel, M. Wegener, and P. Gumbsch, "Tailoring the characteristic length scale of 3D chiral mechanical metamaterials," Extreme Mech. Lett. **32**, 100553 (2019).

[62]A. Kazemi, K. J. Deshmukh, F. Chen, Y. Liu, B. Deng, H. C. Fu, and P. Wang, "Non-local phononic crystals for dispersion customization and undulation-point dynamics," Phys. Rev. Lett. **131**, 176101 (2023).

[63]J. Kishine, A. Ovchinnikov, and A. Tereshchenko, "Chirality-induced phonon dispersion in a noncentrosymmetric micropolar crystal," Phys. Rev. Lett. **125**, 245302 (2020).

[64]Y. Chen, J. L. Schneider, M. F. Groß, K. Wang, S. Kalt, P. Scott, M. Kadic, and M. Wegener, "Observation of chirality-induced roton-like dispersion in a 3D micropolar elastic metamaterial," Adv. Funct. Mater. 2302699 (published online) (2023).

[65]G. W. Milton and A. V. Cherkaev, "Which elasticity tensors are realizable?," J. Eng. Mater. Technol. **117**, 483–493 (1995).

[66]M. Kadic, T. Bückmann, N. Stenger, M. Thiel, and M. Wegener, "On the practicability of pentamode mechanical metamaterials," Appl. Phys. Lett. **100**, 191901 (2012).

[67]T. Bückmann, M. Thiel, M. Kadic, R. Schittny, and M. Wegener, "An elasto-mechanical unfeelability cloak made of pentamode metamaterials," Nat. Commun. **5**, 4130 (2014).

[68]T. T. Wu, Z. G. Huang, T. C. Tsai, and T. C. Wu, "Evidence of complete band gap and resonances in a plate with periodic stubbed surface," Appl. Phys. Lett. **93**, 111902 (2008).

[69]M. M. Samak and O. R. Bilal, "Evidence of zero group velocity at the lowest dispersion branch through local interactions," APL Mater. **12**, 011111 (2024).

[70]A. A. Krushynska and V. V. Meleshko, "Normal waves in elastic bars of rectangular cross section," J. Acoust. Soc. Am. **129**, 1324–1335 (2011).

[71]H. Bjurström and N. Ryden, "Detecting the thickness mode frequency in a concrete plate using backward wave propagation," J. Acoust. Soc. Am. **139**, 649–657 (2016).

[72]A. Glassner, "Frieze groups," IEEE Comput. Graphics Appl. **16**, 78–83 (1996).

[73]M. I. Aroyo, *International Tables for Crystallography* (John Wiley and Sons, 2013).

[74]P. Wang, F. Casadei, S. H. Kang, and K. Bertoldi, "Locally resonant band gaps in periodic beam lattices by tuning connectivity," Phys. Rev. B **91**, 020103 (2015).

09 April 2024 09:37:57